Supplementary Material

Weldable and Electrochemically Stable Composite of Graphene and polyvinylidene fluoride as a Current Collector for Promoting Reversible Lithium Plating/Stripping

Qiang Guo[1,2,3], Shuhui Wang[1], Yimei Li[1], Jin Wang[1], Yong Wu[1], Yanan Yu[1], Shengjie Xia[1], Di Hu[2,4], Binjie Hu[2], Zhenya Ye[1], Xufeng Zhou[1,]*, George Zheng Chen[3,]* and Zhaoping Liu[1,]*

[1] Key Laboratory of Graphene Technologies and Applications of Zhejiang Province and Advanced Li-ion Battery Engineering Laboratory of Zhejiang Province, Ningbo Institute of Materials Technology and Engineering, Chinese Academy of Sciences (CAS), Ningbo, 315201, China

[2] Department of Chemical and Environmental Engineering, The University of Nottingham Ningbo China, 315100, PR China

[3] Department of Chemical and Environmental Engineering, Faculty of Engineering, The University of Nottingham, Nottingham, NG7 2RD, United Kingdom

[4] Advanced Energy and Environmental Materials & Technologies Research Group, The University of Nottingham Ningbo China, Ningbo, 315100, PR China

Xufeng Zhou E-mail: zhouxf@nimte.ac.cn

George Zheng Chen E-mail: george.chen@nottingham.ac.uk

Zhaoping Liu E-mail: liuzp@nimte.ac.cn

Simulation Method. The hexagonal primitive cell was used to model pristine graphene. The linear cell was used to model pristine (PVDF) $-(C_2H_2F_2)_n-$ (n=3). A 1×1×1 k-point mesh, including the G-center, was used to sample the Brillouin zones. The first-principles calculations were performed by density functional theory (DFT) using the Vienna ab initio Simulation Package (VASP) code.[1, 2] The exchange and correlation functions are implemented by the generalized gradient approximation (GGA) of the Perdew-Burke-Ernzerhof function[3]. The thickness of the vacuum layer over 15 Å is set to avoid interactions between adjacent layers. Structures are fully relaxed until the force converged on each atom is less than 10^{-2} eV/Å, and the energy criteria is set to 10^{-6} eV. In all calculations, the plane-wave cutoff energy is set to 450 eV.

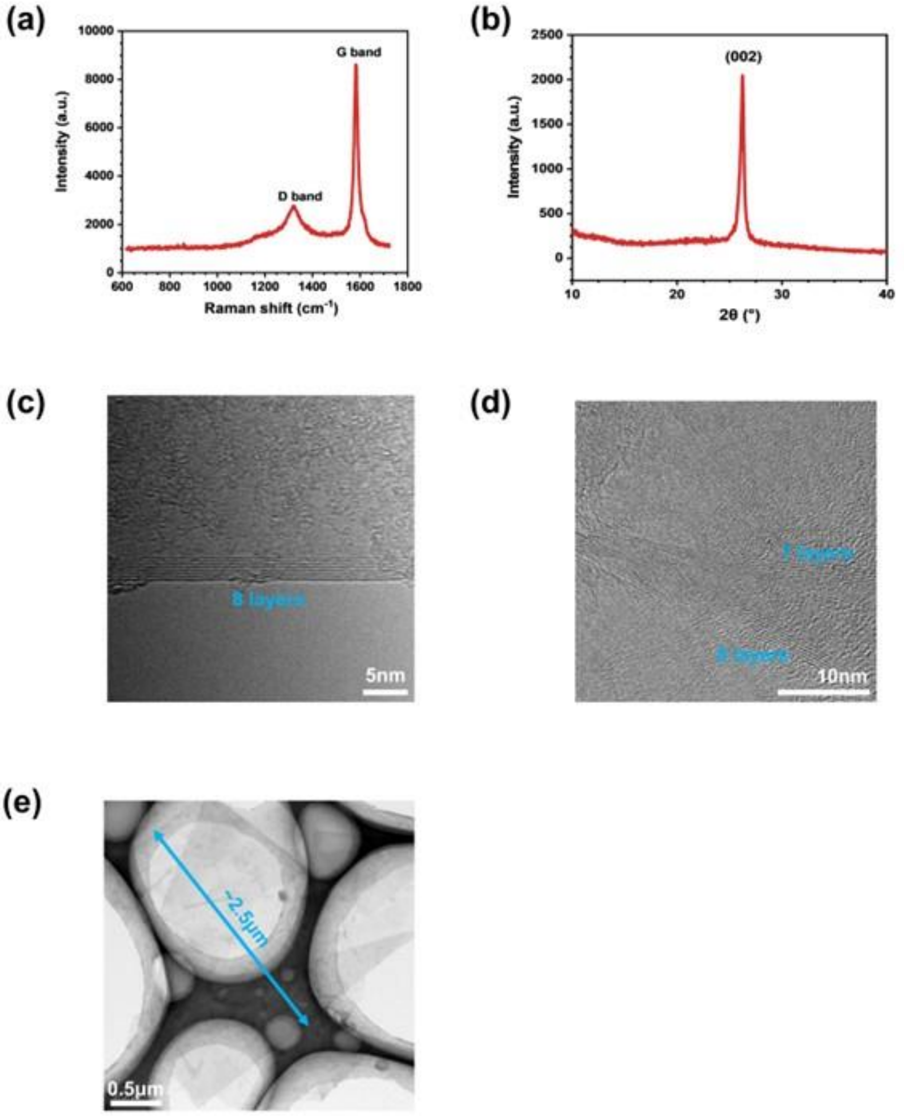

Fig. S1. (a) Raman spectrum, (b) X-ray diffraction pattern of graphene powders. TEM images showing the layer numbers (c-d) and lateral size (e) of graphene sheets.[4]

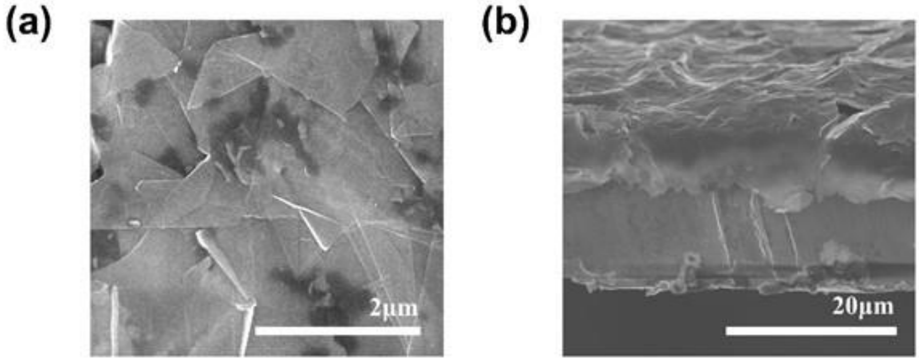

Fig. S2. (a) Top-view and (b) cross-section view SEM images of Gra-0/1-Cu.

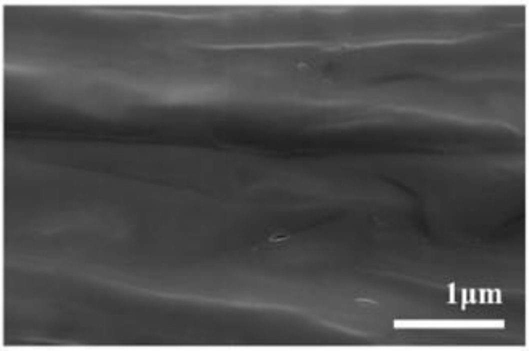

Fig. S3. FIB cross-section view high-magnification SEM images of Gra-5/1.

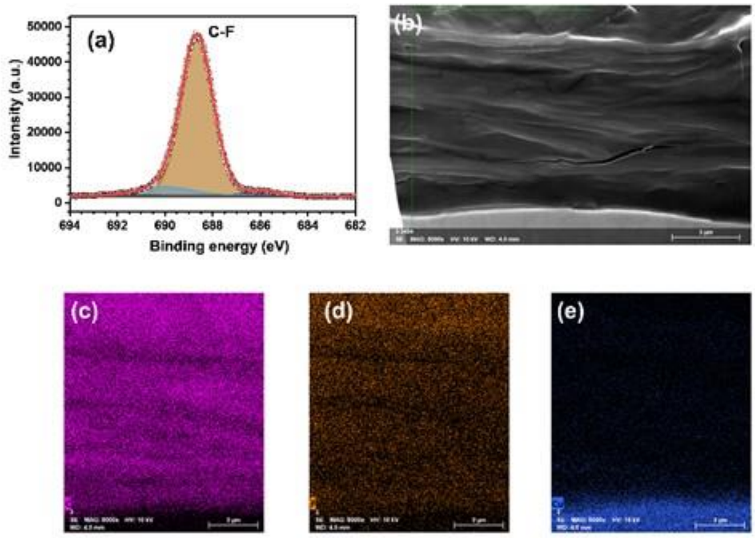

Fig. S4. (a) XPS spectra of the F 1s over the fresh Gra-5/1. EDS mapping of the (b) cross-section view for (c) C, (d) F, and (e) Cu element of Gra-5/1.

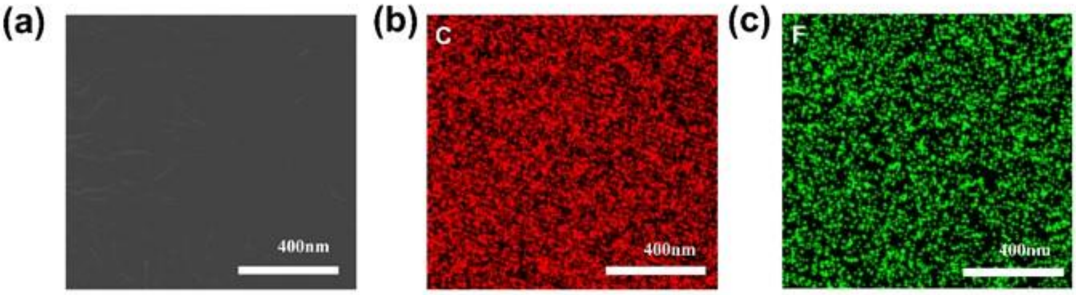

Fig. S5. (a) EDS mapping of the top-view for (b) C and (c) F elements of Gra-5/1.

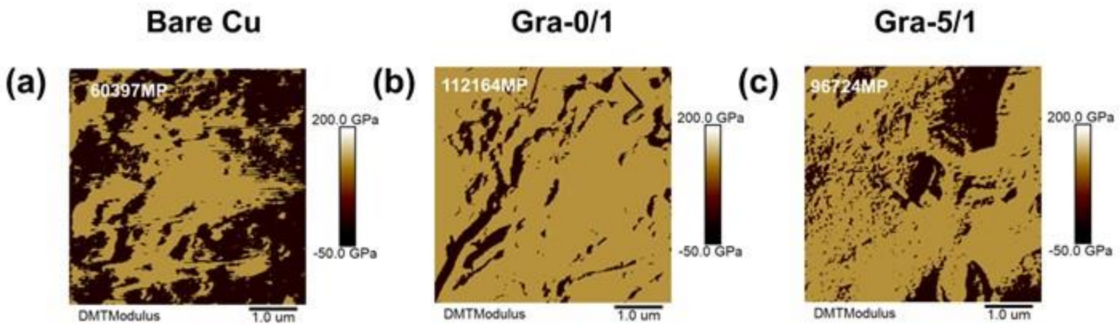

Fig. S6. DMT modulus over (a) bare Cu, (b) Gra-0/1, and (c) Gra-5/1 through AFM characterization.

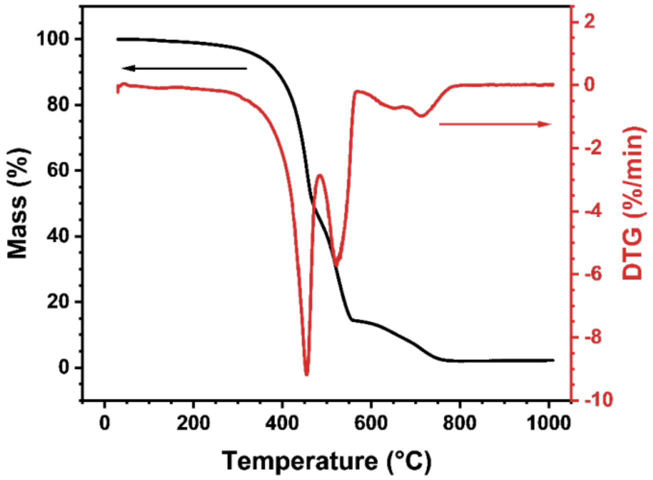

Fig. S7. TGA and corresponding derivative curves of Gra-5/1

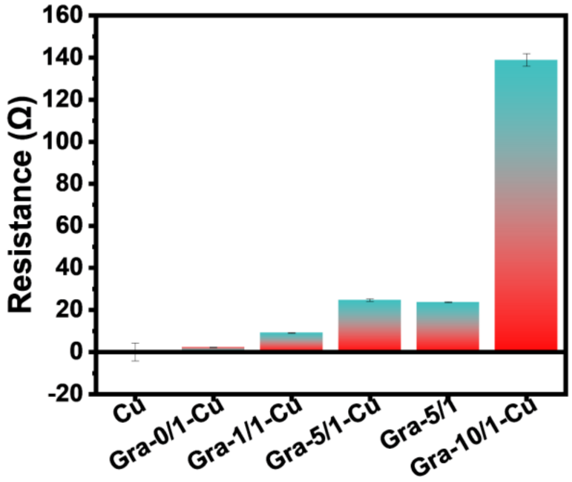

Fig. S8. Resistance of Gra-X/1-Cu (X = 0, 1, 5, and 10), and bare Cu foil.

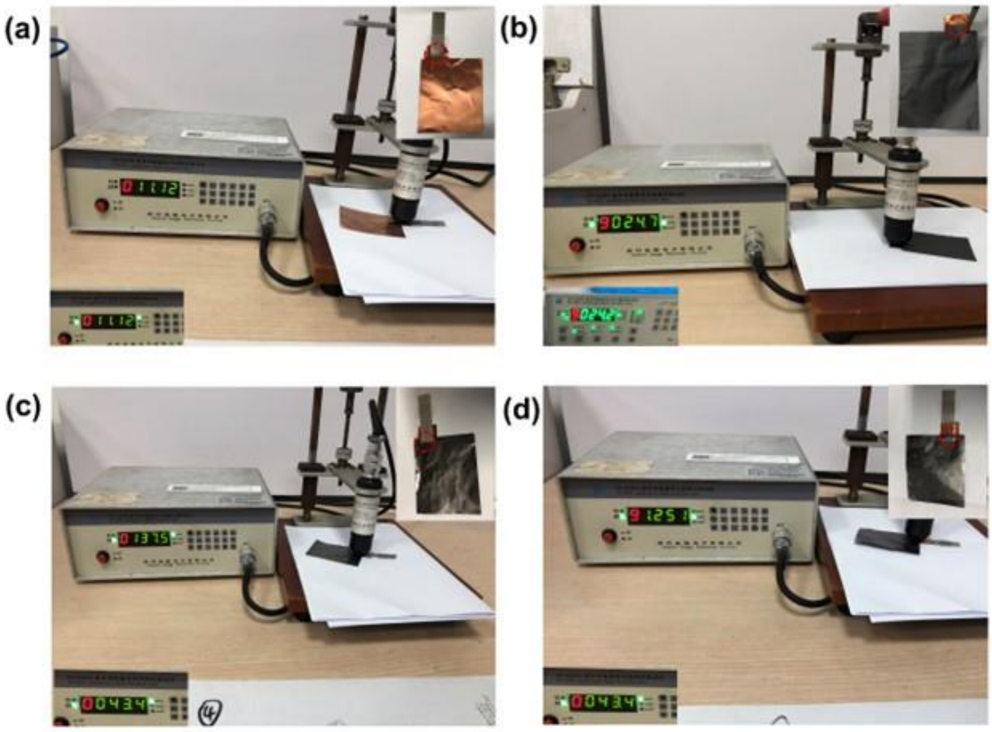

Fig. S9. Contact resistance measurement between (a) bare Cu and metallic tab, (b) Cu and Gra-5/1, (c) graphite paper and metallic tab with silver paste, and (d) graphite paper and Cu sticker. The inset in each image (left lower corner) shows the original resistance of current collectors. Contact resistance is derived from the difference between the contact resistance directly tested and the resistance of the current collector.

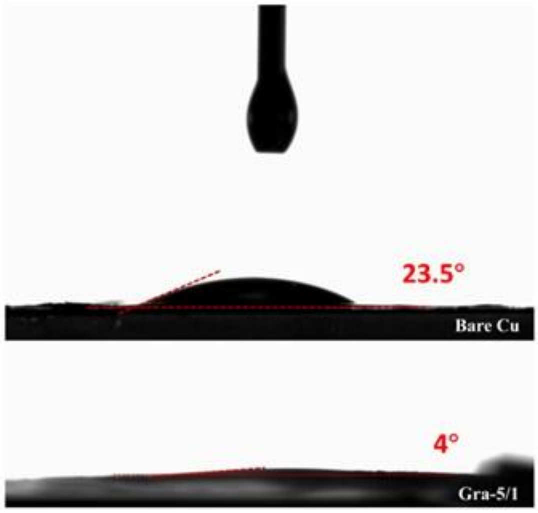

Fig. S10. Contact angles of electrolyte toward Cu foil and Gra-5/1.

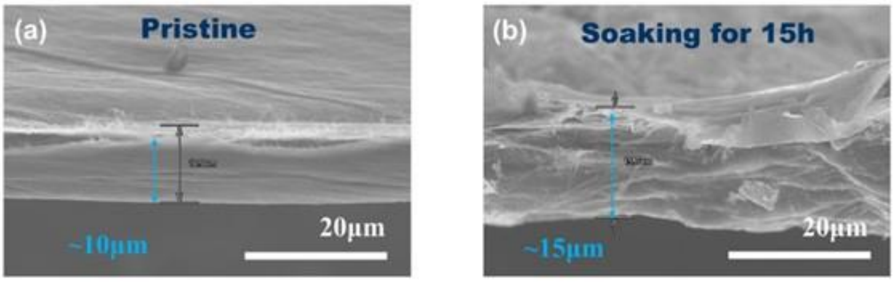

Fig. S11. Cross-section view SEM images of carbon nanotube film (a) before and (b) after soaking in the electrolyte for 15h.

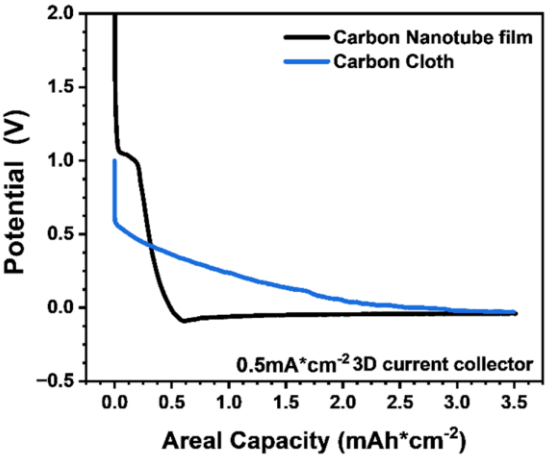

Fig. S12. Voltage profiles of Li plating on carbon cloth and carbon nanotube film with an areal capacity of 3.5 mAh cm^{-2} at 0.5 mA cm^{-2}.

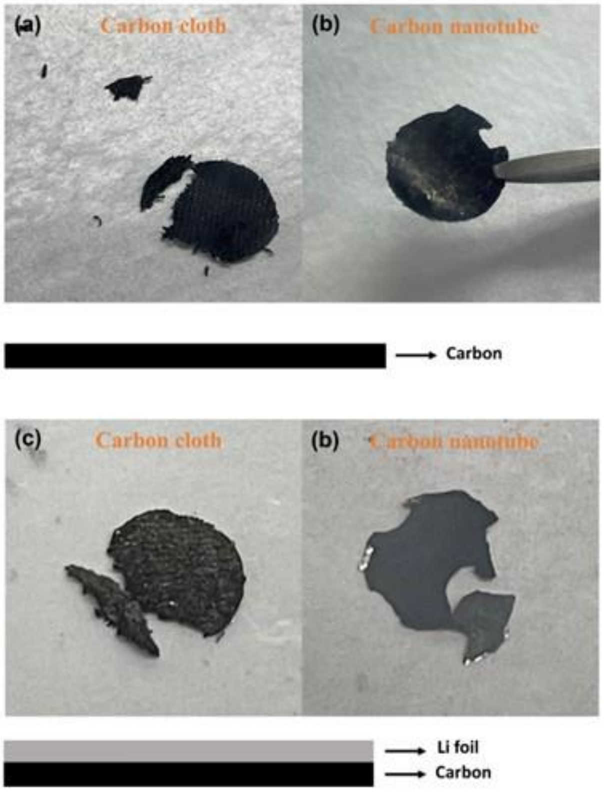

Fig. S13. Optical photograph of carbon cloth and carbon nanotubes film, after (a) and (b) 20 cycles of direct deposition/dissolution and (c) and (d) 30 cycles with Li foil covering on the upper surface at 0.5 mA cm^{-2} with a capacity of 3.5 mAh cm^{-2}.

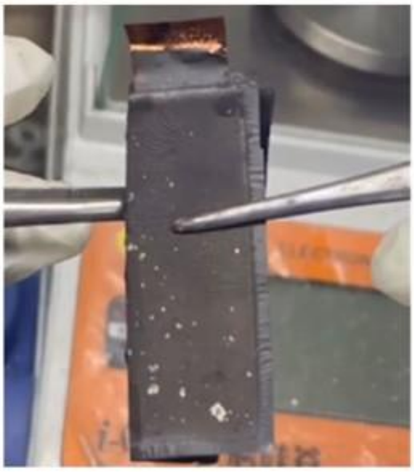

Fig. S14. Optical photograph showing the flexibility of Gra-5/1 after 100 cycles of Li deposition/dissolution in a full pouch cell.

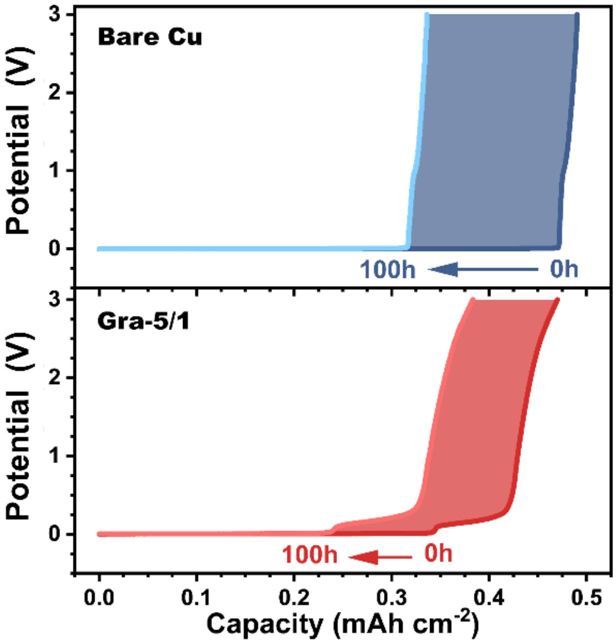

Fig. S15. Potential profiles showing the capacity difference in comparison of galvanic corrosion before and after standing for 100h over the bare Cu and Gra-5/1 with Li plating at 0.01 mA cm^{-2}/0.5 mA cm^{-2} and Li stripping at 0.01 mA cm^{-2}.

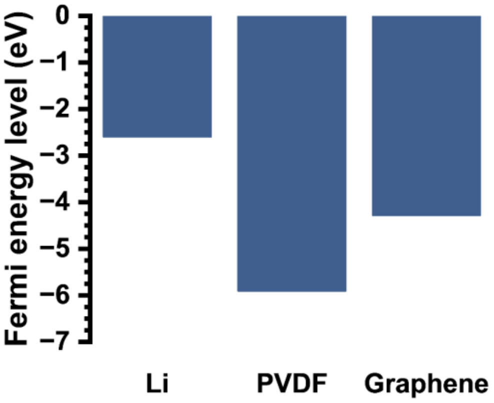

Fig. S16. Simulation result of Fermi energy level of Li, graphene and PVDF.

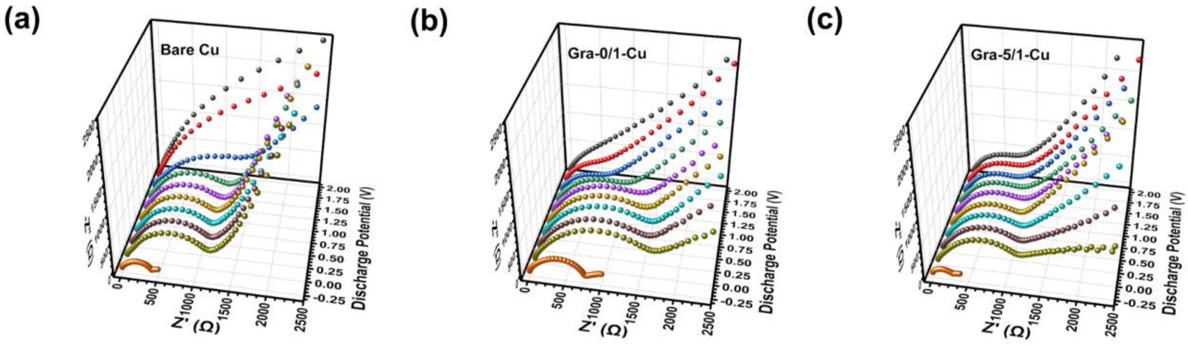

Fig. S17. EIS evolution with discharging from 2V to -0.25V at 0.1 mV·s^{-1} over (a) bare Cu, (b) Gra-0/1-Cu, and (c) Gra -5/1-Cu.

The EIS in the first plating process was measured to explore the SEI evolution on the fresh electrode of Cu, Gra-0/1-Cu, and Gra-5/1-Cu. There are three evident voltage ranges (2 - 1.5 V, 1.5 - 0 V, and 0 - -0.25 V) in the Nyquist plots of bare Cu and Gra-0/1-Cu (Fig. S17a-c), implying that there are three glaring changes in SEI evolution during plating. In the range of 2 V - 1.5 V, the interfacial reaction gradually varies from the double electric layer behavior to the pseudocapacitive-like behavior, which reveals that the formation of initial SEI can break diffusion-limited behavior on the surface of Cu and carbon.[5] With potential decreasing to 0 V, the diameter of the semicircles (R_{ct}) in the high-frequency region gradually increases, because the precursor of SEI or adsorption of active cationic clusters probably hinders the Li^+ diffusion into the surface of the electrode.[6] Finally, when the potential drops to -0.25 V, there is a sharp reduction in the $R_{ct,}$ suggesting that the fast ion transportation channels are formed. By contrast, only two distinct stages (2 - 0 V and 0 - -0.25 V) can be observed in Gra-5/1-Cu. The R_{ct} gradually increases when discharging to 0 V, implying that PVDF is involved in the Li^+ reduction process during the formation of initial SEI. It is noteworthy that the R_{ct} of Gra-5/1-Cu is the smallest among all electrodes when discharging to -0.25 V, revealing that PVDF plays a critical role in the evolution of stable SEI.

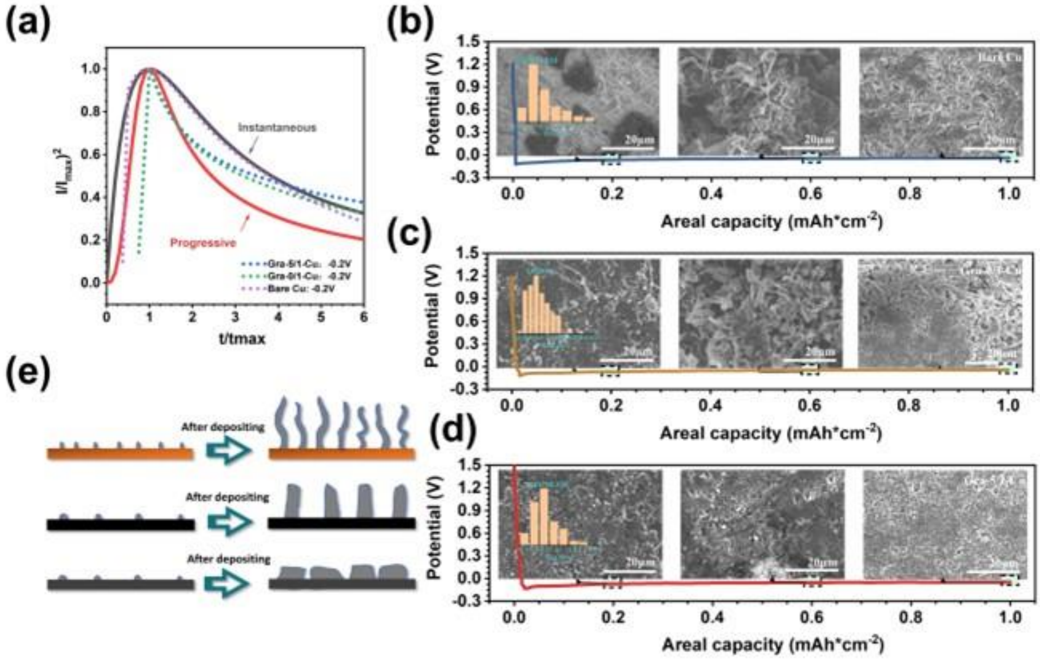

Fig. S18. (a) t/t_{max}-$I/I(_{max})^2$ plots of the fresh bare Cu, fresh Gra-0/1-Cu, and fresh Gra-5/1-Cu. Top-view SEM images of (b) bare Cu, (c) Gra-0/1-Cu and (d) Gra-5/1-Cu electrode after plating with 0.2 mAh cm^{-2}, 0.6 mAh cm^{-2} and 1.0 mAh cm^{-2} of Li. The current density is 0.5 mA cm^{-2}. (e) Li deposition mechanism over bare Cu, Gra-0/1and Gra-5/1.

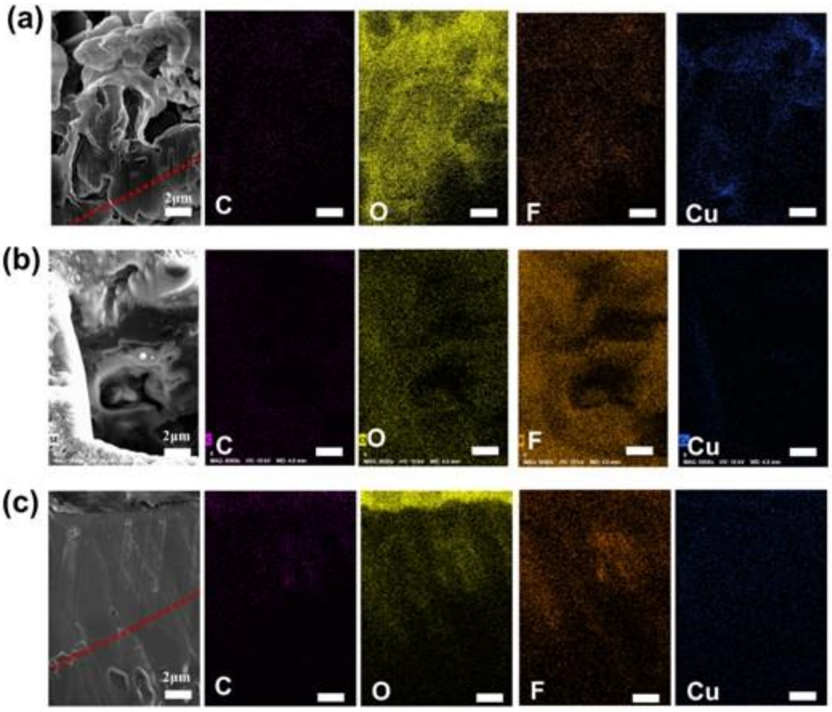

Fig. S19. Cross-section view SEM images and corresponding EDS mapping for C, O, F, and Cu elements of (a) bare Cu, (b) Gra-0/1-Cu, and (c) Gra-5/1-Cu with a plating areal capacity of 3 mAh cm^{-2}. The current density is 0.5 mA cm^{-2}.

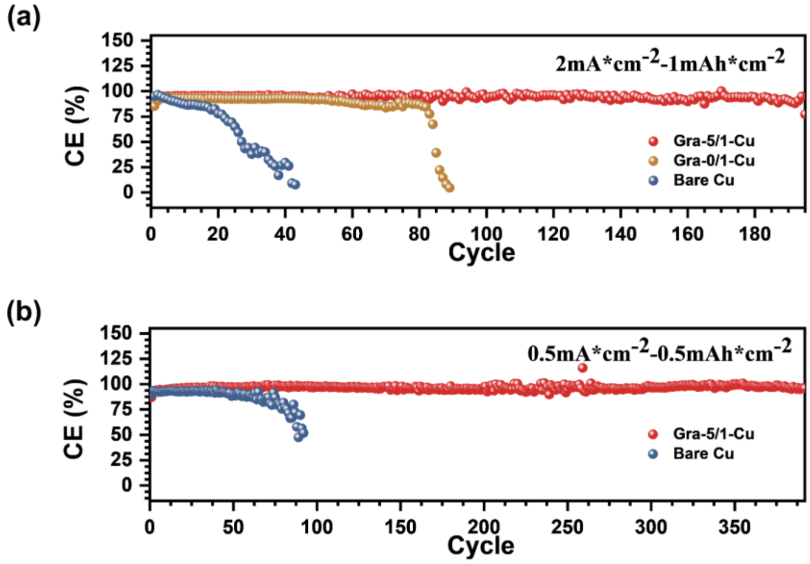

Fig. S20. Comparison of CE of Li plating/stripping with (a) 1 mAh cm^{-2} at 2 mA cm^{-2} and (b) 0.5 mAh cm^{-2} at 0.5 mA cm^{-2} on bare Cu and graphene-based electrodes under ester-based electrolyte.

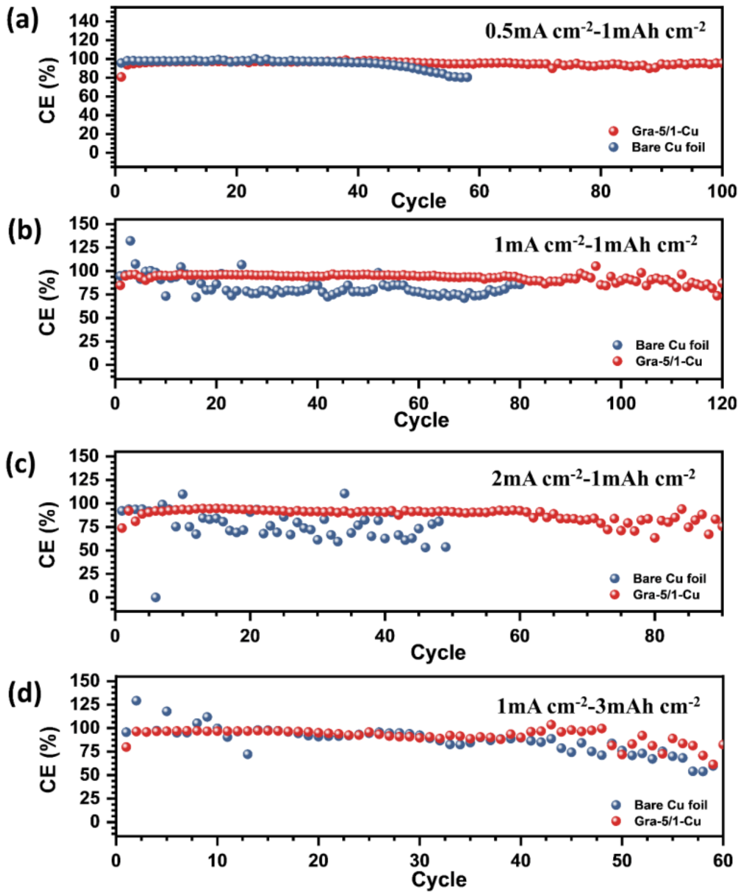

Fig. S21. Comparison of CE of Li plating /stripping with 1 mAh cm^{-2} at (a) 0.5 mA cm^{-2}, (b) 1 mA cm^{-2}, (c) 2 mA cm^{-2} and (d) 3 mAh cm^{-2} at 1 mA cm^{-2} on bare Cu and graphene-based electrodes under ether-based electrolyte.

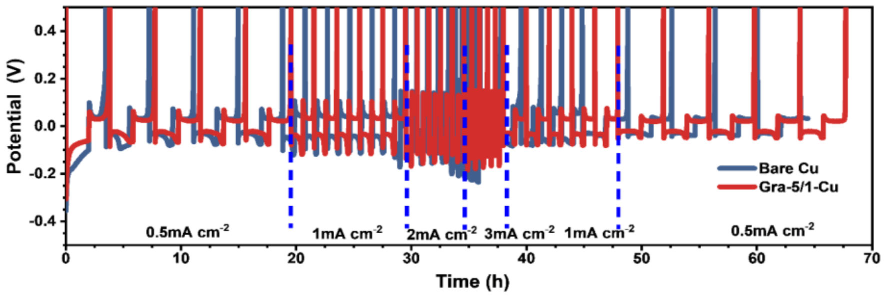

Fig. S22. Comparison of voltage profiles of Li plating/stripping on Cu foil and Gra-5/1-

Cu at different current densities ranging from 0.5 to 3 mA cm^{-2} with an areal capacity of 1 mAh cm^{-2}.

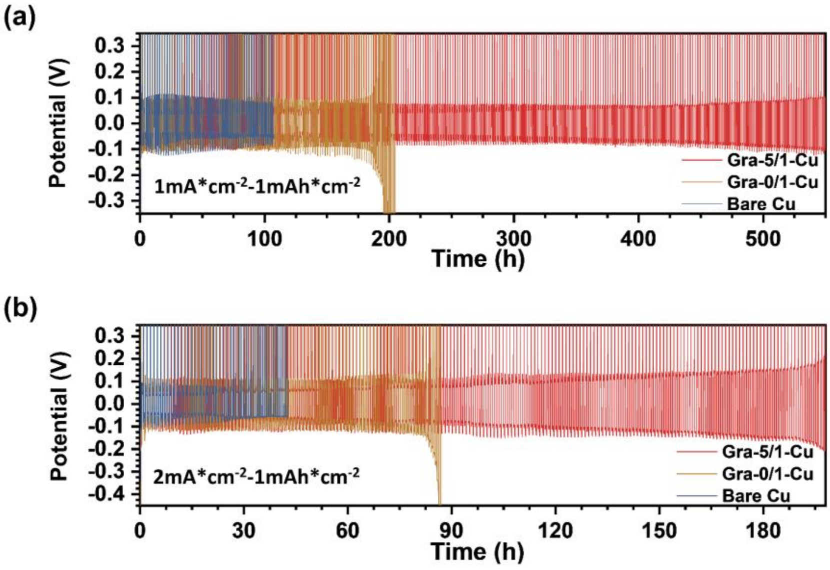

Fig. S23. Voltage profiles of Li plating /stripping on bare Cu foil, Gra-0/1-Cu, and Gra-5/1-Cu with 1.0 mAh cm^{-2} at (a) 1 mA cm^{-2} and (b) 2 mA cm^{-2} under ester-based electrolyte.

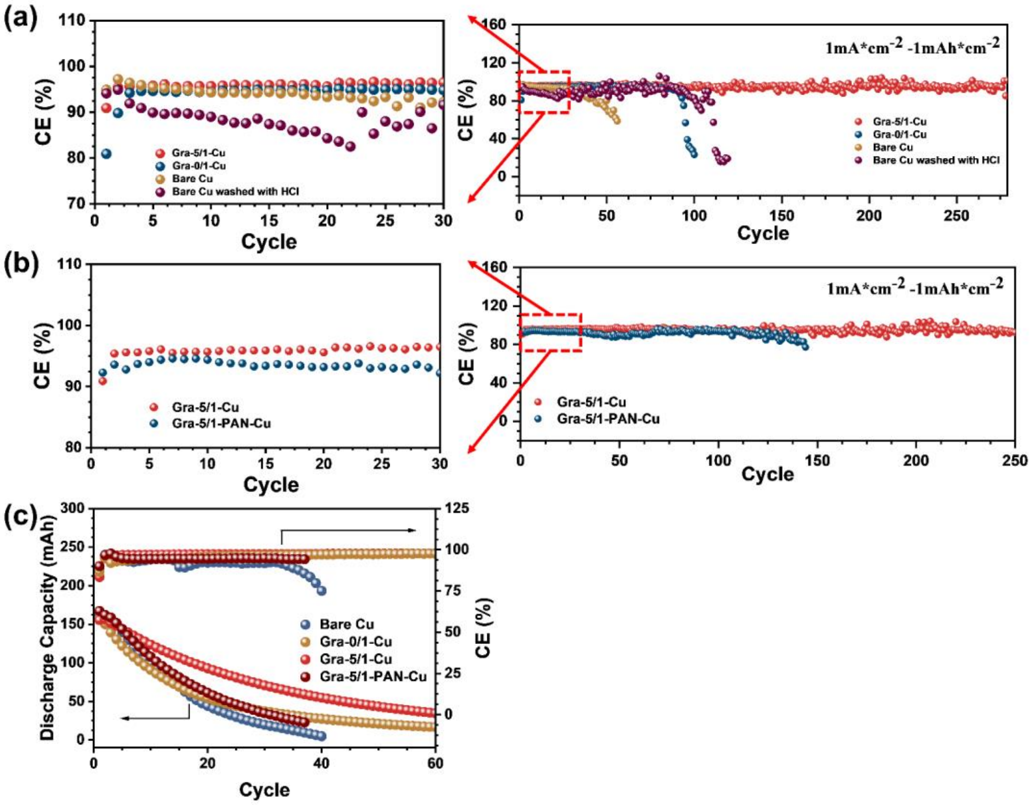

Fig. S24. Comparison of CE of Li plating/stripping with 1 mAh cm^{-2} at 1 mA cm^{-2} over (a) bare Cu, Gra-0/1-Cu, Gra-5/1-Cu, and Cu foil washed with HCl and (b) over Gra-5/1-Cu and Gra-5/1-PAN-Cu. (c) Cycling performance of pouch cells assembled with bare Cu, Gra-0/1-Cu, Gra-5/1-Cu, and Gra-5/1-PAN-Cu current collectors and high areal capacity NCM 811 positive electrodes (~ 4 mAh cm^{-2}).

To clarify the effect of copper oxide or hydroxide which comes from a side reaction between air and Cu on the surface of bare Cu on the cycling performance, the Li||Cu cell was assembled using Cu foil washed with HCl. Fig. S24a shows the cycling lifetime is prolonged, but the CE of the initial cycle for the washed Cu is drastically reduced to 85%. Such a poor CE indicates that the limited active Li in LMFRBs will be significantly consumed by washed Cu. It also verifies the fact that poor cycling of Cu foil is due to the lack of robust and insulating SEI, other than surface contaminant only. In addition, compared with Gra-0/1-Cu, higher initial CE can be found in Gra-5/1-Cu, strongly confirming that PVDF can prevent Li$^+$ from entering the internal area of Gra-5/1 and decrease the formation of initial irreversible Li.

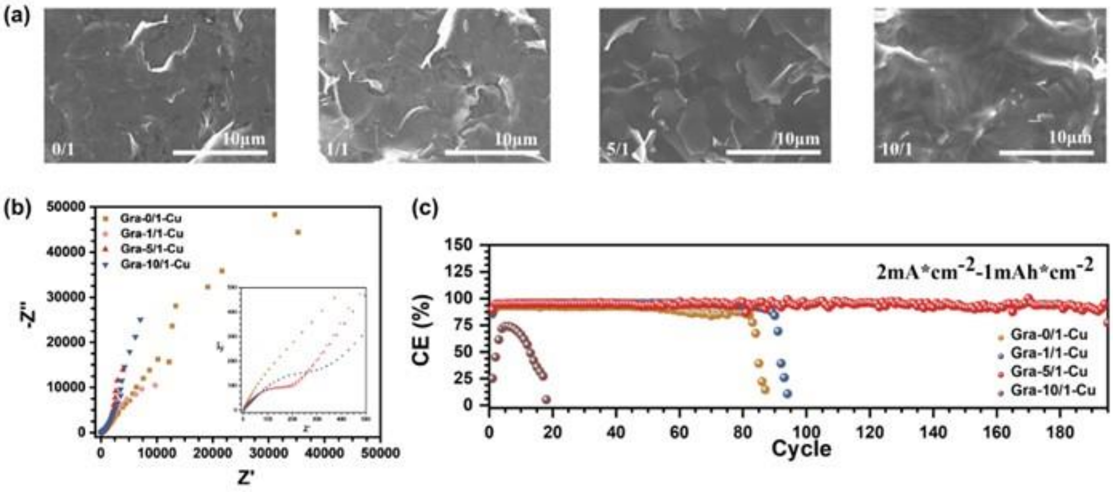

Fig. S25. (a) Top-view SEM images, (b) EIS and (c) coulombic efficiency of fresh Gra-X/1-Cu (X = 0, 1, 5 and 10).

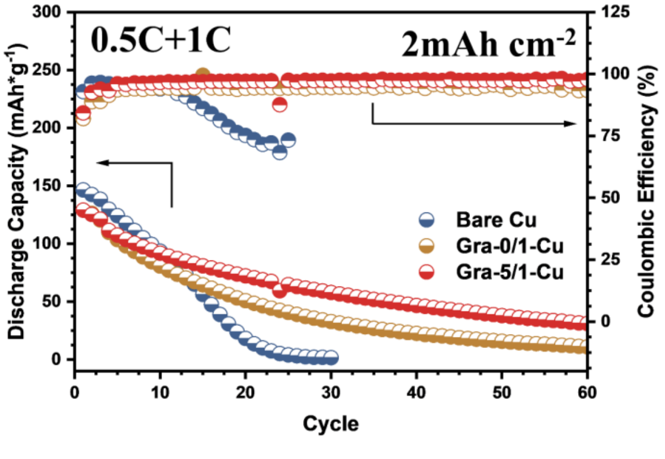

Fig. S26. Cycling performance of negatrode-free Li metal coin full cell assembled with bare Cu, Gra-0/1-Cu, and Gra-5/1-Cu with an areal capacity of ~2 mAh cm^{-2}. 0.5C+1C represents 0.5C charge and 1C discharge.

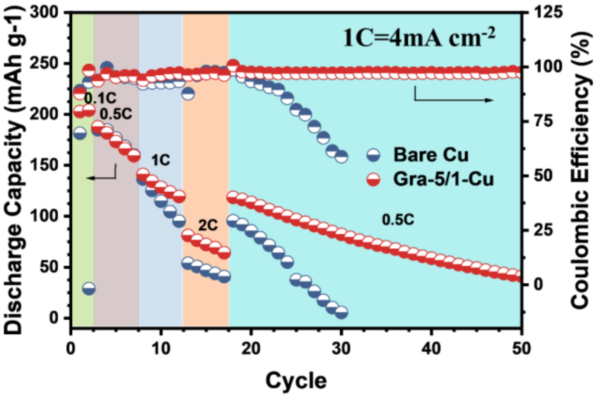

Fig. S27. The rate capability of full cells assembled with bare Cu and Gra-5/1-Cu from 0.1 C to 2 C with an areal capacity of ~4 mAh cm^{-2}.

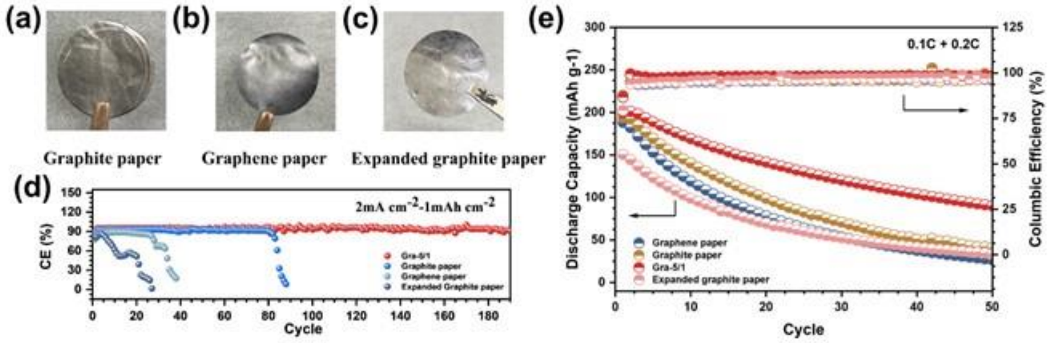

Fig. S28. Optical photographs of (a) graphite paper, (b) graphene paper, and (c) expanded graphite paper. (d) Comparison of CE of Li plating/stripping with 1 mAh cm^{-2} at 2 mA cm^{-2} on Gra-5/1, graphite paper, graphene paper, and expanded graphite paper. Cycling performance of coin full cell assembled with Gra-5/1, graphite paper, graphene paper, and expanded graphite paper current collectors and high areal capacity NCM 811 positive electrodes (~4 mAh cm^{-2}). 0.1C+0.2C represents 0.1C charge and 0.2C discharge.

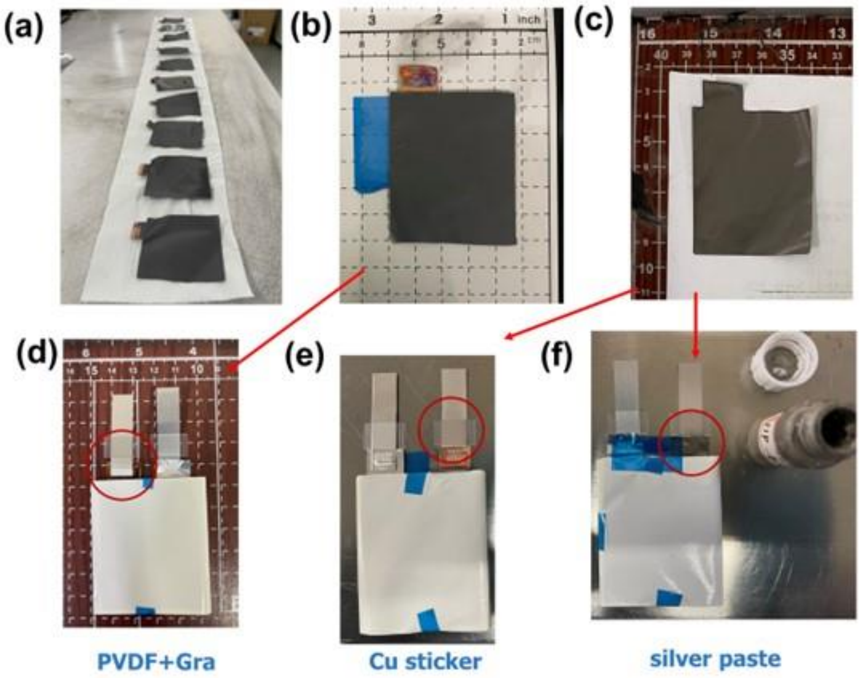

Fig. S29. Optical photographs of (a) large-scale production of Gra-5/1 and (b) related pouch cell scale electrode (47 mm × 57mm). (c) Optical photograph of graphite paper in pouch cell. Optical photographs showing tab connection with Gra-5/1 by welding (d) and graphite paper using Cu sticker (e) and silver paste (f).

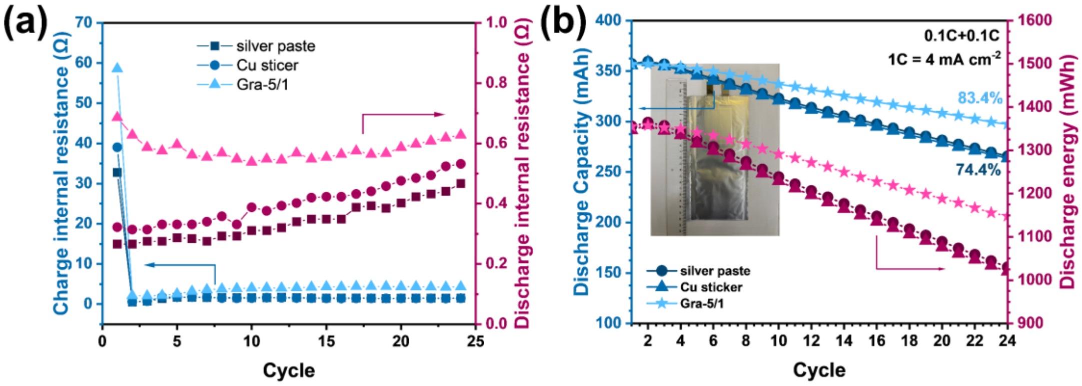

Fig. S30. (a) *In situ* charge & discharge internal resistance profiles and (b) cycling performance of pouch cells assembled with Gra-5/1 and graphite paper current collectors connected by silver paste and Cu sticker and high areal capacity NCM 811 positive electrodes (~ 4 mAh cm^{-2}). 0.1C+0.1C represents 0.1C charge and 0.1C discharge.

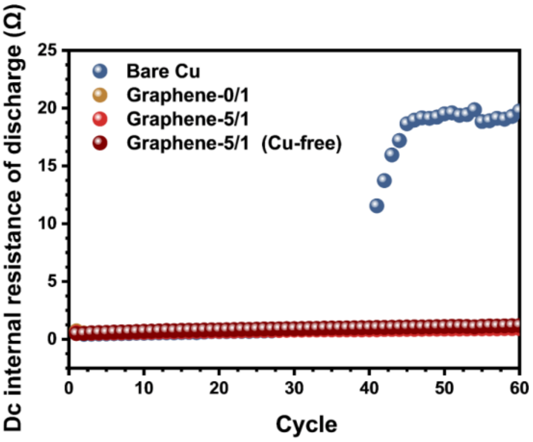

Fig. S31. *In situ* discharge internal resistance profiles of pouch cells assembled with bare Cu, Gra-0/1-Cu, Gra-5/1-Cu, and Gra-5/1 current collectors and high areal capacity NCM 811 positive electrodes (~ 4 mAh cm^{-2}).

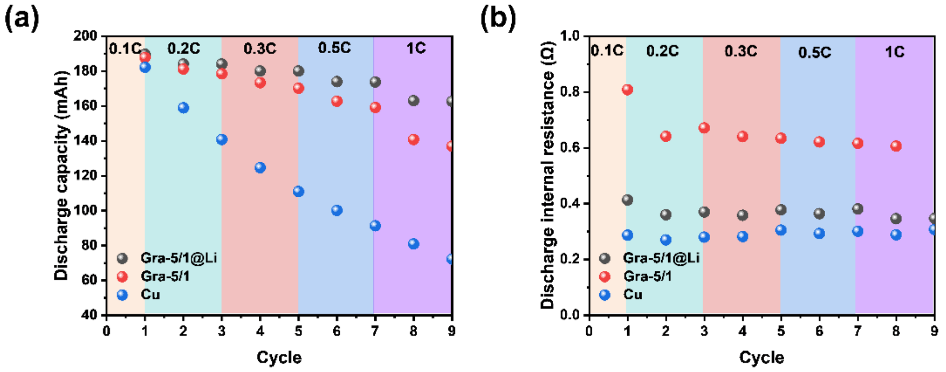

Fig. S32. (a) The rate capability and (b) discharge internal resistance profiles of pouch cells assembled with bare Cu, Gra-5/1@Li and Gra-5/1 from 0.1 C to 1 C with an areal capacity of ~ 4 mAh cm^{-2}.

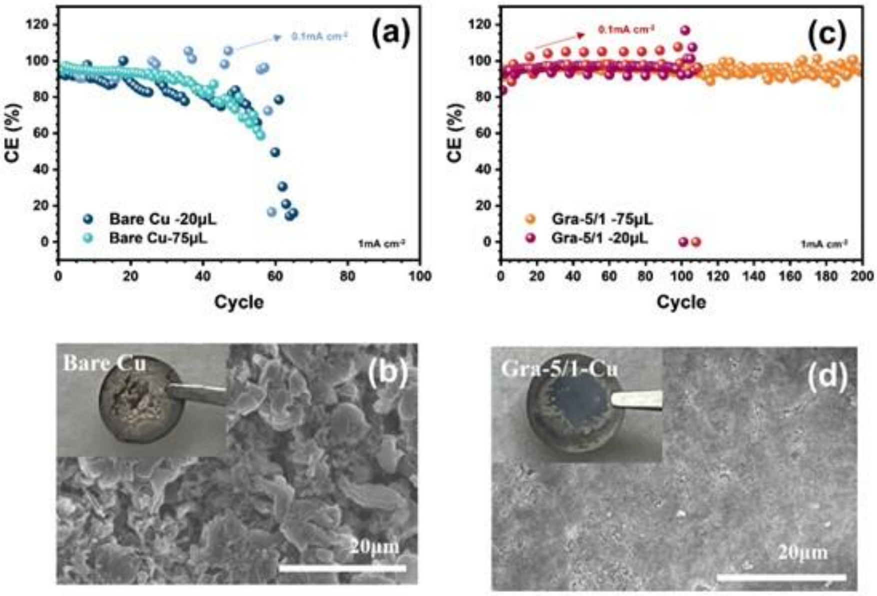

Fig. S33. CE of Li plating/stripping with the capacity of 1 mAh cm^{-2} at 1/0.1 mA cm^{-2} over (a) Cu foil and (c) Gra-5/1 under lean electrolyte conditions (~20 μL). Top-view SEM images of (b) bare Cu and (d) Gra-5/1 after 30 cycles with an areal capacity of 1 mAh cm^{-2} at 2 mA cm^{-2}. The inset of (b) and (d) shows the optical photograph of cycled Cu and Gra-5/1.

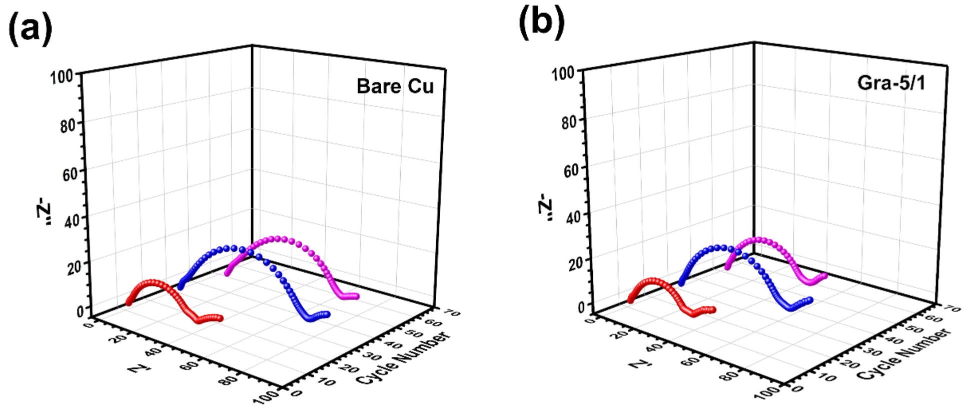

Fig. S34. EIS of (a) bare Cu and (b) Gra-5/1 after 10, 30, and 50 cycles with an areal capacity of 1 mAh cm^{-2} at 2 mA cm^{-2}.

Electrochemical performance is firmly decided by the stability of SEI on the electrode materials. SEI properties such as conductivity on the Gra-5/1 were further collected via EIS (Fig. S34a-b) after cycling. Compared with the bare Cu foil, smaller semicircles in the high-frequency region are obtained in Gra-5/1 after 10, 30, and 50 cycles (Table S3), reflecting that the SEI formed on Gra-5/1 possesses a smaller interface impedance and a smaller R_{ct} than that of the Cu foil. The closer frequency may coincide with SEI resistance (R_{SEI}) and R_{ct}. This result confirms that introduction of PVDF can facilitate the formation of stable SEI with low resistance during Li deposition/dissolution. While higher resistance in SEI formed on Cu foil also renders a negative effect on its electrochemical performance.

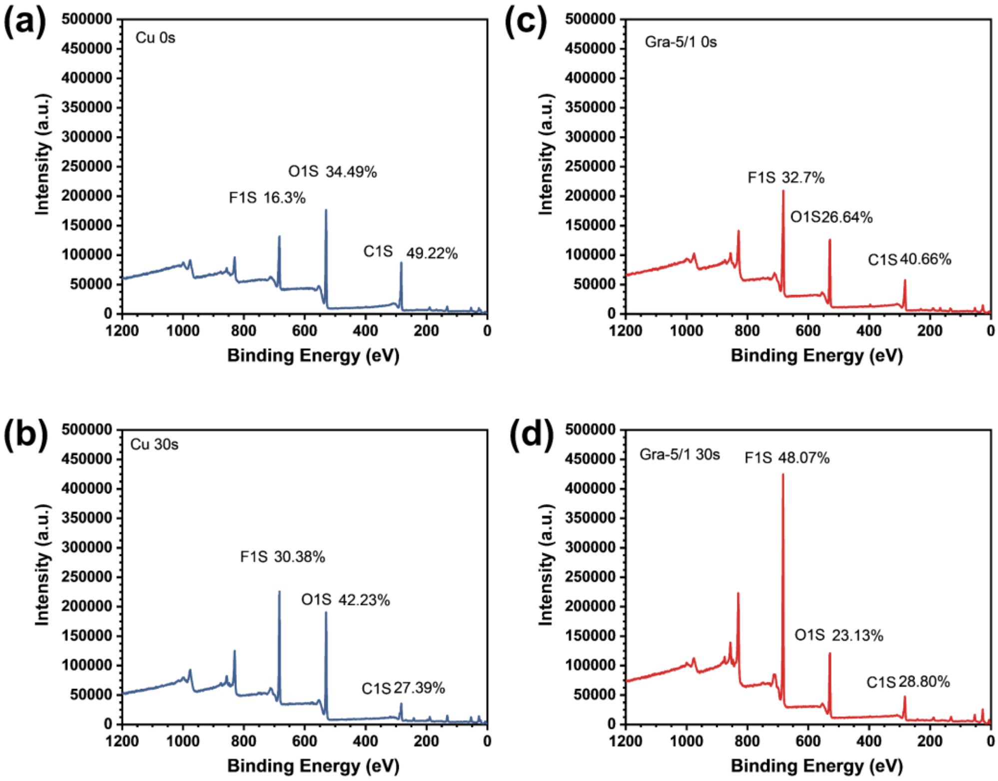

Fig. S35. XPS full spectra at various depths of (a), (b) bare Cu, and (c), (d) Gra-5/1 after 50 cycles of Li plating/stripping with a capacity of 1 mAh cm^{-2} at 2 mA cm^{-2}.

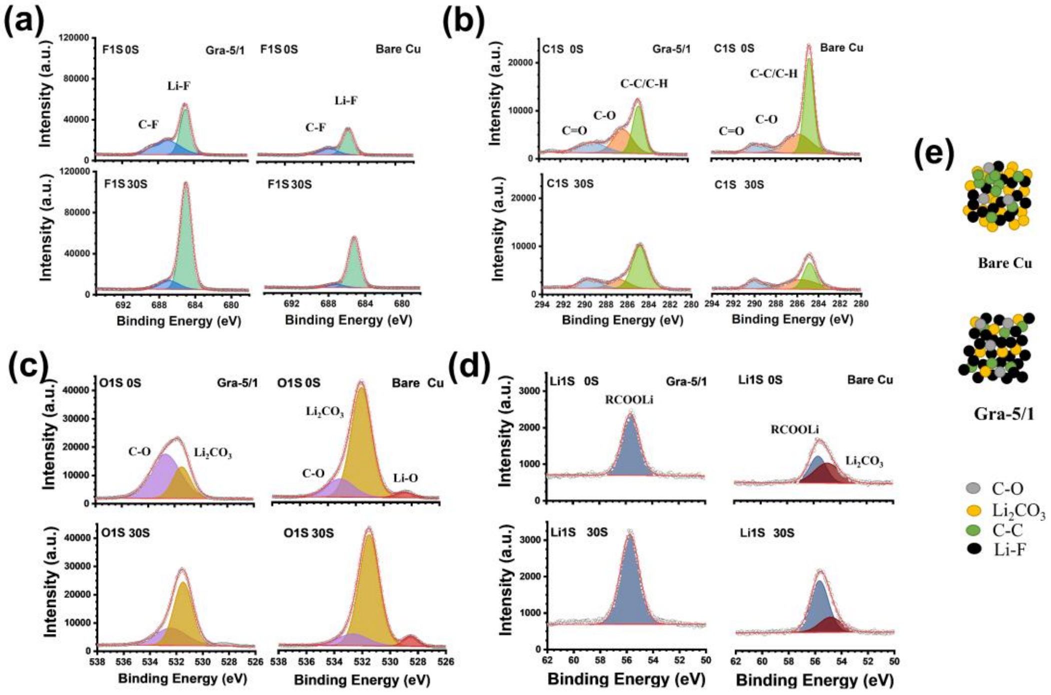

Fig. S36. XPS spectra at different etching depths (0s and 30s) of (a) F 1s, (b) C 1s, (c)

O 1s, and (d) Li 1s of Li plating/stripping with a capacity of 1 mAh cm^{-2} at 2 mA cm^{-2} over the bare Cu and Gra-5/1 after 50 cycles. (e) Illustration of the SEI compositions on the bare Cu (top) and Gra-5/1 (down).

To identify the chemical composition and stability of SEI, the half cells were evaluated after the 50th stripping/plating cycle (1 mAh cm^{-2} at 2 mA cm^{-2}), and the interfacial SEI component was further investigated (Fig. S35 and Fig. S36) at different depth and is displayed graphically in Fig. S36e via XPS. The surface SEI of bare Cu is mainly composed of organic (C–C/C–H) (Fig. S35b) and inorganic (Li_2CO_3) (Fig. S36c) substances. However, Gra-5/1 shows strong peaks of Li-F (Fig. S36a) and RCOOLi (Fig. S36d). Li-F is well-known as a favorable SEI component for its high interfacial energy toward Li and high mechanical strength.[7] Therefore, it efficiently suppresses dendrite growth and contributes to uniform Li deposition. There is a more apparent growth in the intensity of Li-F after 30s' sputtering than the external SEI composition (F1S of Fig. S36a) in the Gra-5/1 compared to the bare Cu, implying that PVDF dispersed in graphene can facilitate the formation of Li-F and help achieve uniform Li deposition/dissolution. Notably, the top surface of the SEI formed in the Cu foil has much stronger C–C/C–H (284.8 eV), C–O (286.2 eV), and C=O (289.5eV) signals compared with Gra-5/1, demonstrating the tremendous electrochemical degradation of organic solvent during cycling (C1s of Fig. S36b). While the intensity of C–C/C–H signal in the internal SEI dramatically reduces, which verifies unstable SEI formed on Cu cannot effectively stop massive electrolyte decomposition contributing to the external higher content of C–C/C–H. The stronger and similar C=O signals can be found in bare Cu before and after Ar sputtering (O1s Fig. S36c) compared to the Gra-5/1's, indicating that both internal and external parts of the SEI contain more organic components resulting from electrolyte decomposition. Therefore, it is indicated that numerous side reactions between the electrolyte and Li can be foreseen in Cu foil-based LMFRBs, which will further accelerate the dendrite formation and capacity attenuation. Compared to Gra-5/1, bare Cu shows a lower RCOOLi content and higher Li_2CO_3 in the Li 1s spectrum (Fig. S36d), implying that the RCOOLi may help Gra-5/1 reduce the electrolyte decomposition. Internal SEI of Gra-5/1 has stronger C=O signals than the external SEI, revealing the electro-reduction of electrolyte may be efficiently inhibited by RCOOLi besides the Li-F. Fig. S35 shows a gradually decreased content of C-C/C-H and Li_2CO_3, an increased amount of Li-F over Gra-5/1, and both increased amounts of Li-F and Li_2CO_3 and decreased content of C-C/C-H for bare Cu along the depth of SEI, suggesting the organic-inorganic feature of hybrid SEI as illustrated in Fig. S36e. It is mainly due to the PVDF-induced Li-F enriched SEI and high electron-retarding ability, which can play a crucial role in improving Li cycling. While vulnerable SEI on Cu will facilitate the formation of Li dendrites and dead lithium.

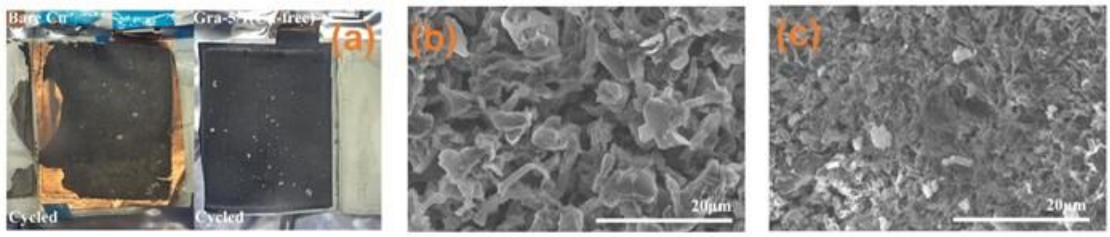

Fig. S37. (a) The optical photographs of bare Cu & Gra-5/1 and top-view SEM images of (b) bare Cu and (c) Gra-5/1 after 100 cycles in pouch cells.

Morphology of bare Cu and Gra-5/1 after cycling was characterized to further clarify how they lose their capacity in pouch cells as illustrated in Fig. S37. Fig. S37a shows that fewer by-products/“dead Li” can be found in the Gra-5/1 after 100 cycles compared with Cu foil, proving that PVDF-induced robust SEI can impressively suppress the generation of Li dendrites. In the LMFRBs, the electrochemically inactive Li species (irreversible capacity) are mainly composed of “dead Li” and by-products. Fig. S37b confirms that the irreversible capacity of Cu-based pouch cell is mainly ascribed to the formation of “dead Li”. While, considering the high CE of Li||C coin cell and reduced “dead Li” (Fig. S37c), the loss of capacity of the Gra-5/1-based pouch cell is probably due to the by-products and the generation of a small part of “dead Li”. Thus, in the practical application, Gra-5/1 contributes to the improvement of cycling performance.

Failure analysis. Failure analysis on Cu-based and Gra-5/1-based batteries were conducted to understand their failure mechanism. Generally, there are three main causes for the failure of LMRBs: 1. depletion of electrolytes; 2. dramatic increase of the internal impedance due to the accumulation of irreversible Li (e.g. “dead Li”); 3. loss of Li inventory.[8] For LMFRBs, loss of Li inventory stems from two possible factors (1. formation of by-products (such as SEI) and 2. formation of “dead Li”).[8] Therefore, Li||Cu half cells with lean electrolyte (~20 μL) and unlimited Li source were assembled to distinguish between factor 1 and 2. To alleviate the “dead Li"-induced dynamic hysteresis, and magnify the effect of the electrolyte, periodic small current densities were applied in the half cell. Fig. S33a shows that the CE of Cu foil decreases obviously after 20 cycles, but after applying a smaller current density, the CE rises back. The Cu foil also exhibits a similar downward trend as shown in the flooded electrolyte condition (75 μL). Then, when a larger current density is applied again (1 mA cm^{-2}), the downward trend of CE does not stop, demonstrating soaring internal resistance is the main factor causing capacity decay. Apparent porous “dead Li” is observed on the Cu foil after 30 cycles (Fig. S33b), showing this growing internal impedance is highly probably caused by the continuous accumulation of “dead Li”. Compared to Gra-5/1-Cu, larger interface impedance on Cu (Fig. S34) after 30 cycles also confirm this “dead-Li”-induced internal resistance can highly block Li-ion transfer.

For the Gra-5/1-Cu, the CE fluctuates regularly with the increase or decrease of the current density in the first 100 cycles (Fig. S33c), but after 100 cycles, CE is almost not affected by the current density and starts fluctuating violently. While Gra-5/1 can run more than 250 cycles in the flooded electrolyte (75μL). Thus, this indicates that electrolyte depletion which is highly ascribed to the formation of by-products may be the main cause of cell failure. Compared to Cu, less bulk-like “dead Li” (Fig. S33d) and smaller interface impedance change (Fig. S34) are discerned on Gra-5/1-Cu after 30 cycles, verifying the formation of by-product could be more tightly related to the capacity decay. These results also confirm the fact that Li dendrite can be efficaciously alleviated on Gra-5/1.

Briefly, apparent dendrite-like Li is deposited on Cu owing to the fragile and proliferating SEI as proved by XPS results after cycling in Fig. S35-S36. Ultimately, whisker-like “dead Li” which can highly hinder the Li-ion transporting will be formed, resulting in exponential failure of the battery. While PVDF-induced Li-F-rich (Fig. S35-S36) and electron-retarding SEI triggers uniform Li ions flux and mitigates the formation of Li dendrites on Gra-5/1. Thus, the formation of by-products and less “dead Li” can lead to slow capacity decay of Gra-5/1-based cells. Thus, for LMFRBs, the loss of Li inventory in Cu-based cells is mainly because of the formation of whisker-like “dead Li”, while the loss of Li inventory in Gra-5/1-based cells is mainly due to the generation of by-products. More persuasively, fewer “dead Li” can be verified in the Gra-5/1-based LMFRB after 100 cycles compared with Cu-based LMFRBs (Fig. S37). How to decrease the by-products/side reaction between Li and electrolyte on Gra-5/1, especially under lean electrolyte conditions is the remaining problem to be tackled.

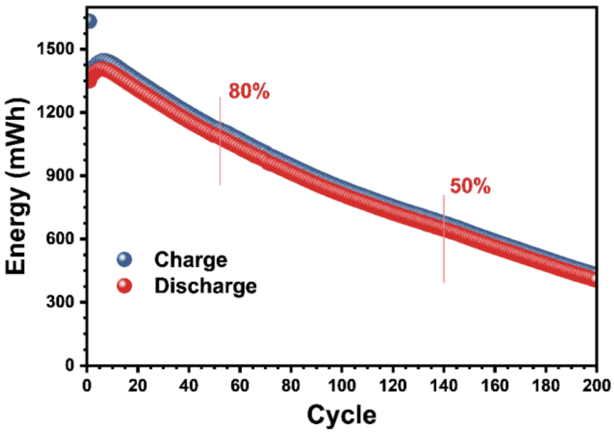

Fig. S38. Charge and discharge energy profiles of LMFRBs assembled with Gra-5/1 and high areal capacity NCM 811 positive electrodes (~ 4 mAh cm^{-2}) using the modified electrolyte.

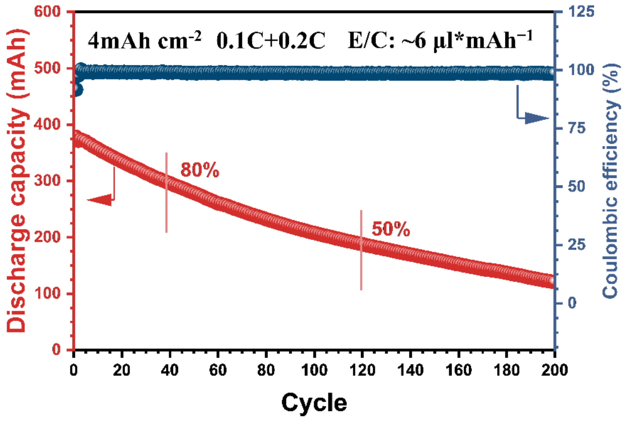

Fig. S39. The discharge capacity profiles of pouch cells assembled with Gra-5/1 and high areal capacity NCM 811 positive electrodes (~ 4 mAh cm^{-2}) using the modified electrolyte (E/C: ~6 μl mAh^{-1}). 0.1C+0.2C represents 0.1C charge and 0.2C discharge.

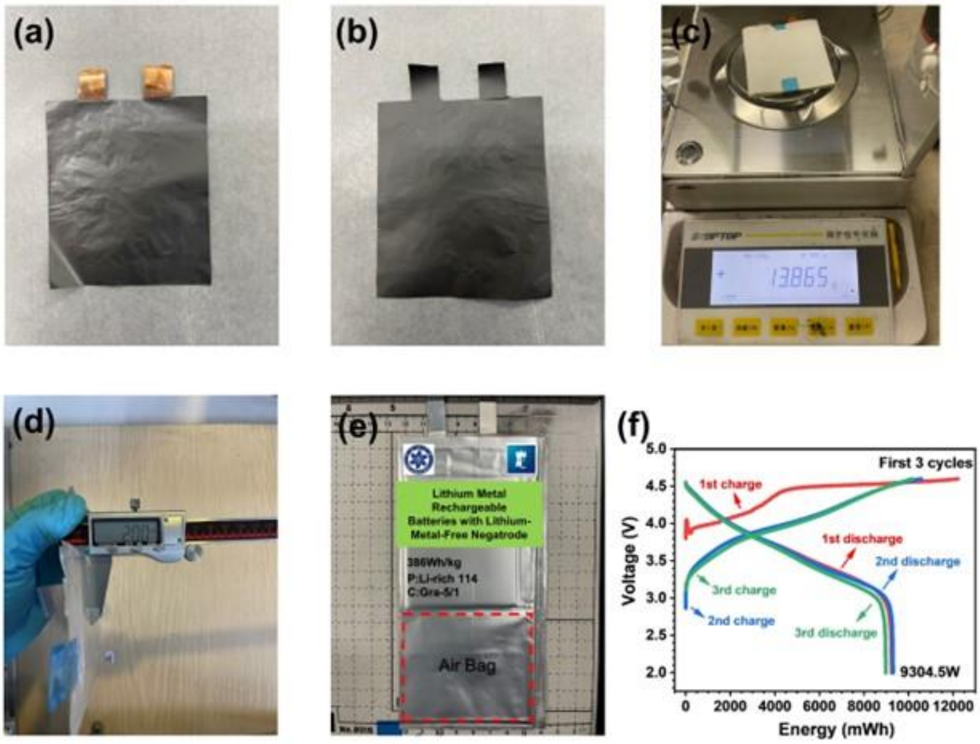

Fig. S40. Optical photographs of the (a) front and (b) back surface of Gra-5/1 current collector (64 mm × 74 mm) used in pouch cells. (c) The mass of the naked pouch cell without packaging, and (d) the thickness, (e) appearance, and (f) the voltage profile for the first 3 cycles of the pouch cell assembled with Gra-5/1 and high areal capacity LR-114 positive electrodes (~ 6 mAh cm^{-2}).

Table S1. Summary of the areal density of different current collectors

Materials	Thickness	Areal density
Cu	~10 μm	~9 mg cm^{-2}
CNT film	~10 μm	~0.46 mg cm^{-2}
Carbon cloth	~300 μm	~10.4 mg cm^{-2}
Graphite paper	~30 μm	~4.6 mg cm^{-2}
Expanded graphite paper	~30 μm	~4.1 mg cm^{-2}
Graphene paper	~30 μm	~3 mg cm^{-2}
Gra-5/1	~10 μm	~2.5 mg cm^{-2}

Table S2. Parameters of a pouch cell assembled with Gra-5/1 and high areal capacity LR-114 positive electrodes (~ 6 mAh cm^{-2}).

Items	Parameter
Pieces of the positive electrode	5
Pieces of Gra-5/1	6
Mass of cell stack/g	13.865 g
Mass of electrolyte (2.4g/Ah)/g	6.43 g
Total mass (no gas bag) /g	24.103 g
Total capacity/Ah	2.601 Ah
Total energy/Wh	9.3045 Wh
Specific energy of cell stack (with electrolyte)/Wh/kg	458.46Wh/kg
Specific energy (no gas bag)/Wh/kg	386Wh/kg
Energy density (no gas bag) /Wh/L	927.5Wh/L

Table S3. Fitting resistance data of galvanostatic plating/stripping in symmetrical cells using Gra-5/1 or bare Cu foil with an areal capacity of 1.0 mAh cm^{-2} at 2 mA cm^{-2}.

Sample	R1 (Ω)	R2 (Ω)
Gra-5/1-10th	3.035	34.37
Bare Cu foil-10th	2.953	38.57
Gra-5/1-30th	4.336	59.28
Bare Cu foil-30th	5.188	72.3
Gra-5/1-50th	5.335	45.07
Bare Cu foil-50th	7.493	64.84

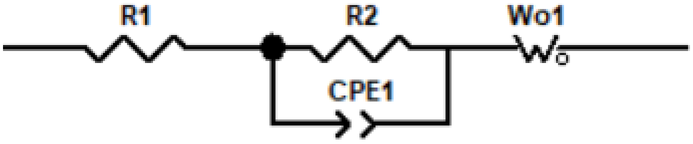

References

1. Kresse, G.; Hafner, J., *Physical Review B* **1994,** *49* (20), 14251-14269.

2. Kresse, G.; Joubert, D., *Physical Review B* **1999,** *59* (3), 1758-1775.

3. Perdew, J. P.; Burke, K.; Ernzerhof, M., *Physical Review Letters* **1996,** *77* (18), 3865-3868.

4. Chen, W.; Jiang, S.; Xiao, H.; Zhou, X.; Xu, X.; Yang, J.; Siddique, A. H.; Liu, Z., *ChemSusChem* **2021,** *14* (3), 938-945.

5. Mathis, T. S.; Kurra, N.; Wang, X.; Pinto, D.; Simon, P.; Gogotsi, Y., *Advanced Energy Materials* **2019,** *9* (39), 1902007.

6. Wang, H.; Feng, X.; Chen, Y.; Liu, Y.-S.; Han, K. S.; Zhou, M.; Engelhard, M. H.; Murugesan, V.; Assary, R. S.; Liu, T. L.; Henderson, W.; Nie, Z.; Gu, M.; Xiao, J.; Wang, C.; Persson, K.; Mei, D.; Zhang, J.-G.; Mueller, K. T.; Guo, J.; Zavadil, K.; Shao, Y.; Liu, J., *ACS Energy Letters* **2019,** *5* (1), 200-206.

7. Xia, L.; Miao, H.; Zhang, C.; Chen, G. Z.; Yuan, J., *Energy Storage Materials* **2021,** *38*, 542-570.

8. Gao, N.; Abboud, A. W.; Mattei, G. S.; Li, Z.; Corrao, A. A.; Fang, C.; Liaw, B.; Meng, Y. S.; Khalifah, P. G.; Dufek, E. J.; Li, B., *Small Methods* **2021,** *5* (2), 2000807.